A Multiscale Scheme for Modeling Catalytic Flow Reactors

Debarshi Majumder and Linda J. Broadbelt
Dept. of Chemical and Biological Engineering, Northwestern University, Evanston IL 60208

DOI 10.1002/aic.11030
Published online November 6, 2006 in Wiley InterScience (www.interscience.wiley.com).

A multiscale modeling approach was developed to capture concentration variations in the fluid in two dimensions for catalytic flow reactors. The methodology couples continuum descriptions of the fluid phase and kinetic Monte Carlo simulations of the catalyst domain. A number of catalytic domains, placed as patches along the length of the reactor, were solved using kinetic Monte Carlo (kMC) and linked with a finite difference (FD) solver for the fluid phase. Patch dynamics concepts, such as lifting, restriction and interpolation, were employed to provide the complete set of boundary conditions to the continuum solver. A simple kinetic mechanism involving adsorption, desorption and a single-step surface reaction was used to validate the approach by comparing the solution obtained using the multiscale scheme with a model solved using a wholly implicit solution. Solutions from a mean-field model and the multiscale scheme for a system in which surface diffusion was low were then contrasted. © 2006 American Institute of Chemical Engineers *AIChE J,* 52: 4214–4228, 2006
Keywords: molecular square catalysts, monolith reactors, membrane reactors, multiscale hybrid technique, kinetic Monte Carlo, patch dynamics, gap-tooth scheme

Introduction

Multiscale modeling has emerged as a major area of interest in materials design.[1–18] The properties of a material used at the process scale are often a consequence of phenomena that occur at different time and length scales. In order to design optimal materials, capabilities to predict the properties at the process scale, based on the phenomena occuring at the relevant scales, are required to keep pace with experimental developments that allow materials to be designed precisely at the nanometer or even atomic scale.[19–34]

One specific area where precise control over material architectures has been accomplished is heterogeneous catalysis. Recently, molecular squares[35] and related materials[19,20,22–30,32] and metal-organic frameworks[36] have been developed that exploit capabilities to direct transition-metal chemistry towards a catalyst with tailored composition and pore structure. Different combinations of metal corners and organic linkers have been shown to yield discrete triangles, squares or extended three-dimensional (3-D) structures having pores or cavities of controlled sizes, with the choice of linkers providing a handle on the specific chemical functionality. These catalytic materials have been supported on membranes with nanometer pore sizes, and have been shown to be stable against leaching.[37] The overall reactor configuration that has been employed is shown in Figure 1. The reactor consists of numerous small cylindrical pores, the inner surface of which is coated with a layer of catalyst. Reactants and products are transported in the fluid phase in both the axial and radial directions, and reaction occurs when molecules contact the catalyst coating on the walls. Although the length scales are smaller, this is the same general configuration as catalytic monoliths or honeycomb reactors that are used in industrial applications.[38–42] Continuum models have already been developed to describe monolith reactors,[43–50] as well as related catalytic membrane reactors.[51–62] Typically, these models have been solved using standard computational-fluid dynamics (CFD) techniques, such as finite difference (FD) or finite element methods (FEM). Very recently, there

Correspondence concerning this article should be addressed to L.J. Broadbelt at broadbelt@northwestern.edu.

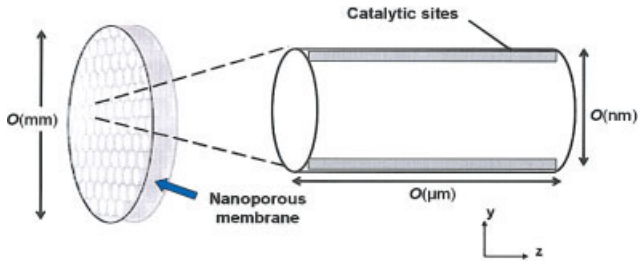

Figure 1. Reactor configuration being examined is a nanoporous membrane, which contains a film of catalytic material along the surface inside the cylindrical pores.

A reactor consists of numerous pores as shown on the left. The enlarged view of a single pore is shown on the right side. The reactants are transported in the fluid phase, contact the active catalytic sites on the wall of the pores, and are transformed into products. [Color figure can be viewed in the online issue, which is available at www.interscience.wiley.com.]

has been an effort to develop specialized techniques to improve the efficiency of the solution of these models.[60,63] However, these continuum-level simulations have assumed that the catalytic surfaces are spatially homogeneous. Therefore, mean-field kinetic models have been used. These models are inadequate to handle the presence of defects, facets, impurities, reconstructions and lateral interactions that can render heterogeneous surfaces nonuniform. In these cases, it is necessary to use a molecular-level solver to describe the catalytic surface.

Recently, a small number of models have been developed for heterogeneous-catalytic reactors which link a molecular-level solver for the catalyst phase with a macroscopic-scale solver for the fluid phase.[64–67] However, all these models have assumed that the concentration in the fluid phase varies in only a single direction, normal to the plane of the catalytic surface, and, thus, are not able to describe the axial concentration gradients inherent in monolithic and membrane reactors. Given the current approaches, it would be computationally prohibitive to solve a catalyst domain long enough to experience a concentration variation in the contacting fluid.

This work describes the development of a multiscale approach that couples a continuum description of the fluid phase and kinetic Monte Carlo simulations of the catalyst domain using the concept of patch dynamics[3,4,7,8,11,12] to handle the concentration variation in the axial direction. The governing equations and parameters in the fluid phase were specified based on representative conditions for liquid-phase olefin epoxidation using catalytic assemblies of molecular squares supported over membranes with nanometer pore sizes. First, contributions of the different modes of transport in the fluid phase for these representative conditions were evaluated in order to develop an appropriate model to describe the transport of reactants and products in the fluid phase. The fluid phase model was solved using finite difference, and coupled to the catalytic surface via a number of catalytic domains, placed as patches along the length of the reactor, that were solved using kinetic Monte Carlo (kMC). Patch dynamics concepts, such as lifting, restriction and interpolation, were employed to provide the complete set of boundary conditions to the continuum solver. Two different reaction mechanisms were evaluated to demonstrate the approach. A simple kinetic mechanism involving adsorption, desorption and a single-step surface reaction was used to validate the solution obtained using the multiscale scheme by comparison with a model solved using a wholly implicit scheme. The second mechanism included a bimolecular surface reaction step between surface species that were considered to be immobile, so that the solution from the multiscale method and a mean-field description could be contrasted.

Model Development

The reactor consists of a catalytic film fashioned on an inert support as depicted in Figure 1. Reactants enter the reactor through transport in the axial direction and come in contact with the catalytic surface through diffusion in the radial direction. Products are formed on the surface which then diffuse out to the fluid phase, and are then transported out of the reactor to the downstream side.

Transport in fluid phase

Formulation of the governing equations describing the concentration of reactants and products in the fluid phase requires knowledge of the dominant modes of transport in the fluid. The different possible modes of transport in a pore are Knudsen, molecular and surface diffusion, and Poiseuille flow. Knudsen diffusion occurs when the mean free path of the molecules is of comparable size to or larger than the pore diameter. Molecular diffusion occurs when the molecules collide with each other more frequently than the walls of the pores, that is, the mean free path is shorter than the dimensions of the pore. Surface diffusion is an activated process that takes place on the surface of the pores. Poiseuille flow, or convection, is pressure dependent, and takes place only when the pore diameter is significantly larger than the size of the mean-free path of the molecules. Each of the transport modes can be expressed in terms of a diffusivity as shown in the Eqs. 1–4.[68] In this analysis, surface diffusion was assumed to be negligible, because the pores will be filled with liquid and the radial distribution function will likely be uniform.

$$\text{Knudsen diffusion} \quad D_K = \frac{2}{3} r \sqrt{\frac{8RT}{\pi m}} \tag{1}$$

$$\text{Molecular diffusion} \quad D_M = \frac{1.173x10^{-16}(\phi M_B)^{1/2} T}{\mu V_A^{0.6}} \tag{2}$$

$$\text{Surface diffusion} \quad D_{surface} = D_{surface,\infty} \exp\left(\frac{-E_s}{RT}\right) \tag{3}$$

$$\text{Poiseuille flow} \quad D_{Poiseuille} = \frac{pr^2}{8\eta} \tag{4}$$

where r is the pore radius in m, m is the weight of a molecule in g, T is the temperature in Kelvin, ϕ is an association parameter,[69] M_B is the molecular weight of the solvent B (kg/kg mol), μ is the viscosity of the solvent B (kg/m s), E_s is the activation energy for surface diffusion, R is the universal gas constant, p is the average pressure in Pa, and η is the

Table 1. Parameters Used to Determine Contributions of the Different Modes of Transport in a Nanoporous Membrane

	Styrene	Dichloromethane
Molecular weight (kg/kg mol)	104	85
η (kg/m s)	6.75×10^{-4}	4.17×10^{-4}
ρ (g/ml)	0.9	1.32

Styrene and dichloromethane were used as a representative solute and solvent, respectively, at a temperature of 300 K.

viscosity of the solvent in Pa-s. Equation 2 is the widely used Wilke-Chang equation for diffusion in liquids. Other correlations, such as the Rankin equation,[70] were tested and shown to give molecular diffusion coefficients of the same order of magnitude.

The overall transport is a combination of all these individual components, and the Knudsen and molecular contribution can be calculated based on the Pollard and Present approximation[71] shown as follows:

$$D_{Total} = \frac{1}{\frac{1}{D_K} + \frac{1}{D_M}} + D_{Poiseuille} + KD_{surface} \tag{5}$$

where K is the partition coefficient between the fluid and the surface.

Based on the epoxidation of styrene at 300 K using iodosylbenzene as the oxidant and dichloromethane as the solvent, representative diffusion coefficients were calculated to determine the dominant mode of transport as a function of pore diameter and average pressure. The parameters used in Eqs. 1–4 are summarized in Table1, and the contribution of convective flow to the total flow is plotted in Figure 2. For pores 20 nm in dia., which is currently the lower bound of commercially available nanoporous alumina disks, convection was found to account for 65 to 80% of the total transport for pressures ranging from 1 to 2 atm. For larger pore sizes, and also for higher-pressures, convection will have an even greater contribution. Based on these calculations, the steady-state governing equation in the fluid phase was formulated as follows

$$u\frac{\partial C_{i,fluid}}{\partial z} = D_{iL}\frac{\partial^2 C_{i,fluid}}{\partial y^2} \tag{6}$$

where u is the local velocity in the fluid phase, $C_{i,fluid}$ is the concentration of the i^{th} component, and $D_{i,L}$ is the diffusivity of the i^{th} component in the fluid. Based on the structure of the pores and the low Reynolds number for the system, the velocity profile in the fluid was assumed to be laminar.[63]

The boundary conditions for the problem are shown as follows:

$$C_{i,fluid} = C_{i,0} \quad y > 0, \; z = 0 \tag{7}$$

$$\frac{\partial C_{i,fluid}}{\partial y} = 0 \quad y = y_{cent}, \; z \geq 0 \tag{8}$$

$$D_{iL}\frac{\partial C_{i,fluid}}{\partial y} = k_{a,i}C_{i,fluid}\left(1 - \sum_{j=1}^{n}\theta_j\right) - k_{d,i}\theta_i f(\theta_i, \theta_j, \ldots\ldots, \theta_n, T) \;\; y = 0, \;\; z \geq 0 \tag{9}$$

where $k_{a,i}$ and $k_{d,i}$ are the adsorption and desorption constants of species i, respectively, θ_i is the surface coverage of species i, and n is the total number of surface species. In this equation, the adsorbates have been assumed to occupy one site for simplicity. The function $f(\theta_i, \theta_j, \ldots\ldots, \theta_n, T)$ represents the effect of lateral interactions and the microstructure of the surface. If the surface model is based on mean-field kinetics, f takes a value of unity. However, if a molecular model such as kinetic Monte Carlo is used, f takes a value different from unity, depending on the nature of the kinetic mechanism and the microstructure of the surface. It may be noted that Eq. 9 is valid only for species which exist in both free and adsorbed forms. For a species which directly participates in the surface reaction steps in the free form, the flux at the interface is given by its net rate of formation per unit area of the catalytic surface, an example of which is shown later in the context of a bimolecular kinetic mechanism.

Kinetic models on the surface

Two different reaction mechanisms were used as test cases. The first one involved a unimolecular surface reaction shown as follows:

$$A + S \rightleftharpoons AS \tag{10}$$

$$AS \rightleftharpoons BS \tag{11}$$

$$BS \rightleftharpoons B + S \tag{12}$$

where A and B represent the reactant and product species, respectively, S represents an empty lattice site on the surface, and AS and BS are the adsorbed forms of A and B, respectively.

The second kinetic mechanism involved two different reactant species A and B adsorbing on the surface and a bimolecular surface reaction step leading to the formation of

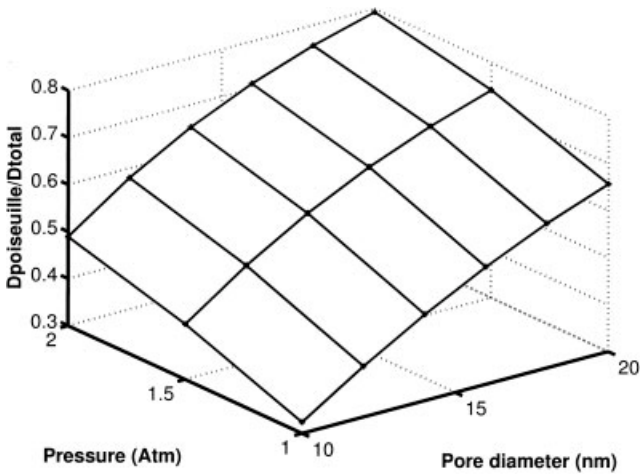

Figure 2. Contribution of convective mode of transport in the axial direction in pores ranging from 10 to 20 nm as a fraction of the total transport.

The operating pressure ranges from 1 to 2 atm. For the smallest commercially available pore dia. of 20 nm, convection is found to account for about 65–80% of the total transport. For larger pore sizes and higher pressures, convection will have an even bigger contribution.

Table 2. Rate Constant Parameters for the Unimolecular Surface Reaction Mechanism in Eqs. 10–12

Reaction	Forward Reaction k_f	Reverse Reaction k_b
10	4000[a]	481[b]
11	33.0[b]	0.01[b]
12	289[b]	3200[a]

[a]molecule/M/site/s.
[b]molecule/site/s.

the product C, which exists only as a free species in the fluid phase.

$$A + S \rightleftharpoons AS \tag{13}$$

$$B + S \rightleftharpoons BS \tag{14}$$

$$AS + BS \rightleftharpoons C + 2S \tag{15}$$

The sets of kinetic parameters for these mechanisms are summarized in Tables2 and 3. For the unimolecular mechanism, the parameters were modified from previous work on lattice-based kMC.[72] For the bimolecular mechanism, the parameters were derived from the same work, but the adsorption and desorption rate coefficients were increased to reduce computational time.

Mean-field Surface Model. In the mean-field (MF) model, the adsorbed molecules are assumed to be distributed homogeneously. The quantity of interest in this model is the fractional coverage θ, which is continuous ranging between 0 and 1. For the unimolecular mechanism described by Eqs. 10–12, the coverages at steady state are described by the following set of algebraic equations.

$$\begin{aligned} k_{aA}C_{A,fluid}\left(1-\sum_{j=1}^{n}\theta_j\right) - k_{dA}\theta_A - k_{Sf}\theta_A + k_{Sb}\theta_B = 0 \\ k_{aB}C_{B,fluid}\left(1-\sum_{j=1}^{n}\theta_j\right) - k_{dB}\theta_B + k_{Sf}\theta_A - k_{Sb}\theta_B = 0 \end{aligned} \tag{16}$$

where k_{Sf} and k_{Sb} are the forward and reverse rate constants for the surface reaction, respectively, k_{aA} and k_{aB} are the rate constants for adsorption of A and B, respectively, and k_{dA} and k_{dB} are the rate constants for desorption of A and B, respectively.

For the bimolecular mechanism described by Eqs. 13–15, the following set of algebraic equations describes the coverages at steady state for the mean-field model.

$$\begin{aligned} k_{aA}C_{A,fluid}\left(1-\sum_{j=1}^{n}\theta_j\right) - k_{dA}\theta_A - k_{Sf}\theta_A\theta_B \\ + k_{Sb}C_{C,fluid}\left(1-\sum_{j=1}^{n}\theta_j\right)^2 = 0 \\ k_{aB}C_{B,fluid}\left(1-\sum_{j=1}^{n}\theta_j\right) - k_{dB}\theta_B - k_{Sf}\theta_A\theta_B \\ + k_{Sb}C_{C,fluid}\left(1-\sum_{j=1}^{n}\theta_j\right)^2 = 0 \end{aligned} \tag{17}$$

For this mechanism, the mean-field approximation is clearly seen in the surface reaction steps, where the forward and backward rates are given by $k_{Sf}\theta_A\theta_B$ and $k_{Sb}C_{C,fluid}(1-\sum_{j=1}^{n}\theta_j)^2$, respectively. The inherent assumption embedded in these rate expressions is that all lattice sites on the surface are equally accessible to an adsorbate molecule, which implies an infinite rate of surface diffusion. Under working conditions on a real catalyst surface, however, an adsorbate molecule on the surface can interact only with a finite number of neighboring sites, depending on the rate of surface diffusion.

Kinetic Monte Carlo Surface Model. Due to its ability to explicitly track individual events such as adsorption, desorption, reaction and diffusion, and also because of the ability to track the individual molecules and their positions on the catalytic surface, kinetic Monte Carlo provides a more descriptive method of studying the evolution of coverage that includes spatial information. It is specifically valid in situations where the continuum description fails and can account for heterogeneities in the local environment on the surface. In particular, kinetic Monte Carlo can easily track events that are impacted by adsorbate-adsorbate interactions and situations where low surface diffusion is present, both of which a mean-field model has difficulty handling.

The kMC model for the unimolecular mechanism described by Eqs. 10–12 is identical to the MF model, where the coverage values are calculated using the numbers of lattice sites occupied by a given adsorbate divided by the total number of lattice sites. For the bimolecular mechanism described by Eqs. 13–15, low-surface diffusion has been assumed, and a given adsorbate molecule is assumed to interact only with its nearest neighbor sites. Thus, at a given coverage and fluid-phase concentration, both the forward and reverse rates of surface reaction are lower than $k_{Sf}\theta_A\theta_B$ and $k_{Sb}C_{C,fluid}(1-\sum_{j=1}^{n}\theta_j)^2$, respectively, as predicted by the MF model. The forward rate is tallied by counting the number of AS-BS ensembles on the surface. It may be interesting to note that for this bimolecular mechanism, the flux of product C at the interface, which is given by the net rate of the surface reaction step, is likely to be predicted differently by the MF and the kMC models at a given coverage and fluid-phase concentration. Since the interfacial flux is used as the boundary condition for the fluid phase solver, the resulting profile of the product C in the fluid phase can be expected to be different.

Fully Implicit Solution

The fully implicit model for the given reactor configuration was implemented in order to provide a benchmark for

Table 3. Rate Constant Parameters for the Bimolecular Surface Reaction Mechanism in Eqs. 13–15

Reaction	Forward Reaction k_f	Reverse Reaction k_b
13	1.0[a]	0.107[b]
14	1.0[a]	0.357[b]
15	2.22[b]	0.0

[a]molecule/M/site/s.
[b]molecule/site/s.

Table 4. Parameters Used for all Problems

Parameter	Units	Value
Diffusivity in fluid	m^2/s	5.3×10^{-9}
Fluid thickness	m	1.0×10^{-8}
Fluid velocity	m^2/s	0.01
Grid size in radial direction	m	2.4×10^{-10}

the multiscale solution. The fully implicit model consists of simultaneously solving the fluid transport model, described by Eq. 6, along with the set of algebraic equations derived from the mean-field models for the kinetic schemes considered, which are obtained from Eqs. 16 or 17. The resulting set of differential-algebraic equations (DAEs) was solved using a second-order finite-difference scheme using central difference in the radial (y) direction, and backward difference in the axial (z) direction. The parameters corresponding to the solution of the fluid phase are shown in Table4. The fully implicit model includes all the assumptions inherent to the mean-field approximation. For the unimolecular reaction mechanism, the mean-field model should match perfectly with the kinetic Monte Carlo model, and, therefore, the fully implicit solution can be used to validate the implementation of the multiscale scheme. In the case of the bimolecular mechanism, for low surface diffusion rates, the fully implicit solution should predict a higher conversion of A and B if the multiscale scheme is properly implemented.

Multiscale Coupling

A small number of models have been developed in the past to link a molecular-level solver for the catalyst phase with a macroscopic scale solver for the fluid phase.[64–67] However, these models are not suitable for an accurate description of small tubular shaped reactors, such as nanoscale membrane reactors or monoliths, because resolution of concentration in these models only occurs in a single direction, perpendicular to the plane of the lattice.

The present multiscale method builds on previous work in which a molecular-level solver for the catalyst phase was coupled with a macroscopic solver for the fluid phase,[64–67] but augments these previous approaches by allowing for resolution of concentration gradients in two spatial directions. The different components of the multiscale model developed in the current work are described later. The coupling scheme used to combine these components is then discussed. All results were obtained for a pore 20 nm in dia. and 1 μm in length.

Components

Finite Difference Scheme. A second-order finite difference scheme with 43 grid points per component in the radial direction spaced 0.24 nm apart for each axial location was used to solve the steady-state problem described in Eq. 6. The number of grid points was selected based on decreasing the grid size and monitoring when the solution asymptotically converged within a tolerance of 1.0×10^{-6} M for all species. A backward difference scheme in the axial direction allowed the solution to march in the axial direction in steps of 0.01 μm starting from the set of concentration boundary conditions at the inlet point of the reactor. The backward difference scheme allowed for upwinding, which made the solution particularly memory efficient, while still retaining the desired accuracy. The boundary conditions at the catalytic surface were obtained based on the solution of the surface model, as well as the restriction operations which are discussed later. An iterative scheme, discussed later in this section, was implemented to obtain the final solution.

Kinetic Monte Carlo. An efficient lattice-based kinetic Monte Carlo solver[72] was further augmented to solve for steady-state profiles. In this scheme, three possible events, adsorption, desorption and surface reaction, were considered. An efficient algorithm was used to update the transition probabilities. Further details of the implementation of the lattice-based kMC solver are given by Dooling and Broadbelt.[72]

In order to simulate low surface diffusion, only first nearest-neighbor interactions were considered between adsorbate molecules. Periodic bounday conditions were implemented to minimize the effects of the finite lattice sizes. For each set of kinetic parameters considered, different lattice sizes were used to determine the smallest size above which the lattice size was found to have no significant effect on the solution.

The overall solution methodology consisted of an iterative scheme in which the fluid conditions were varied, and kinetic Monte Carlo was used as a tool to evaluate the steady-state surface conditions and interfacial flux for a given fluid phase condition. Because kinetic Monte Carlo is a stochastic-solution method, its output is characterized by fluctuations. As a result, when kMC is used to solve for steady-state profiles, identification of the steady-state coverage is not as straight-forward as when a mean-field model is used. In order to overcome this issue, a second-order linear filter[65] was implemented which was capable of rejecting a significant portion of the noise and produced a smoother profile. The state-space representation of the filter is as follows:

$$\frac{dy_F}{dt} = y_{kMC} \tag{18}$$

$$\frac{dy_{kMC}}{dt} = \frac{K}{\tau}(y_{kMC} - y_F) - \frac{1}{\tau}y_{kMC} \tag{19}$$

where y_{kMC} is the output of the kMC simulator, y_F is the filter output, K is the filter gain, and τ is the time constant. Figure 3 shows the results obtained using the parameters $\tau = 0.5\ s$ and $K = 1$ (dimensionless) for the unimolecular mechanism described by Eqs. 10–12 with a fluid-phase reactant concentration of 8 M at the interface and a 30×30 lattice. The filter output was found to oscillate initially around the kMC output, but the oscillation quickly dampened to produce a smoother profile. Time-averaged profiles for each species are monitored at every 1 s interval in order to identify steady state. If the maximum variation in the time-averaged profiles relative to the minimum time-averaged value is less than a specified tolerance over a period of 4 s, steady state was deemed to have been attained. A tolerance of 1% was used for all the runs.

The size of the lattice structures that can be simulated using molecular solvers such as kMC with reasonable computational expense are on the order of 10^3 sites. However, based on experimental evidence obtained by our collabora-

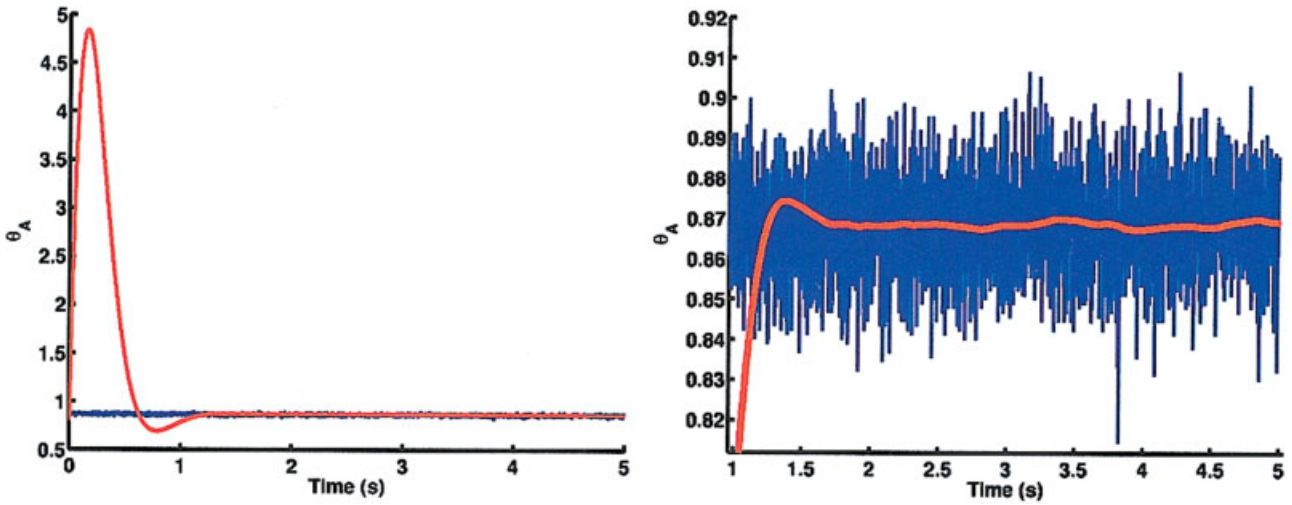

Figure 3. Effectiveness of a second-order linear filter in eliminating stochastic noise for the identification of steady state.

The noisy line represents the output of the kMC solver, while the smoother line represents the filter output. A 30 × 30 lattice was used for the unimolecular mechanism with fluid-phase concentrations of 8 M and 0 M for A and B, respectively, and initial surface coverages of A and B both equal to 0. The figure on the left shows the evolution of the coverage of A as a function of time, while the figure on the right is a magnified view of a portion of the profile seen on the left. The filter parameters K and τ were set to 1 and 0.5 s, respectively. The filter output was found to oscillate initially around the kMC output, but rapidly stabilized to produce a smooth profile. [Color figure can be viewed in the online issue, which is available at www.interscience.wiley.com.]

tors,[37] a single pore can contain more than 10^6 catalytic sites on the surface, which makes it prohibitively expensive to simulate. Because the concentration in the fluid phase in contact with different sites varies, it is not sufficient to use a simple scaling factor to convert between the lattice size simulated and the total number of catalytic sites in the entire reactor as done for reactors with homogeneous fluid phases, such as batch or CSTR.[72] A gap-tooth scheme was used to overcome this challenge as described later.

Gap-tooth Scheme. Recently developed by Kevrekidis et al., the gap-tooth scheme[3,4,7,8,11,12] allows two different levels of description to coexist in a computational domain. In this scheme, the domain is decomposed into periodically-spaced modules, each having width "h", called teeth, which can be solved using a certain suitable level of description. The spaces between the teeth are called gaps, with a width "H", in which a solution may be obtained by using a coarser level of description than that used in the teeth. Each tooth in the domain corresponds to a nodal point for the coarse solution. Details of the implementation of this scheme are described by Kevrekidis and coworkers,[3,4,11,12] but some of the features most pertinent to our implementation are described here. In the gap-tooth scheme implemented here, each tooth is solved using the microscopic descriptor kinetic Monte Carlo, while the coarse description is based on interpolation techniques.

Figure 4 shows how the gap-tooth scheme was implemented. The catalytic surface of the pore was divided into small modular regions, or teeth, each consisting of a 30 × 30 lattice, which were solved using the kMC solver. The configuration of the lattice sites was initialized by "lifting" based on the steady-state coverage obtained in these lattice sites during the previous iteration. During lifting, adsorbed species are randomly placed on the lattice sites in such a way that the fractional occupancy of a given species in the lattice exactly conforms to its coverage. In the most simple case in which no coverage gradient on the surface needs to be taken into account, such as the ones implemented here, the positions of the adsorbed species on a given 30 × 30 lattice can be chosen randomly without constraints. However, if a coverage gradient exists on the surface, special care needs to be taken to ensure that the gradient is replicated at the mi-

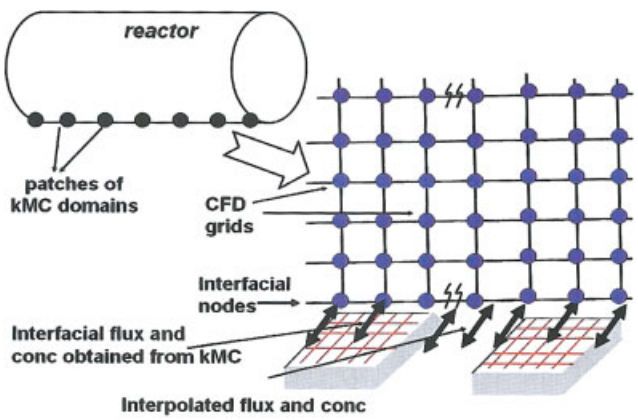

Figure 4. The multiscale coupling method implemented using a gap-tooth scheme.

The catalytic surface was decomposed into small discontinuous patches which were solved separately using a kMC solver. The interfacial concentration and flux boundary conditions were obtained for the entire length of the reactor using restriction and interpolation techniques, which were used as the boundary conditions for the fluid solver. [Color figure can be viewed in the online issue, which is available at www.interscience.wiley.com.]

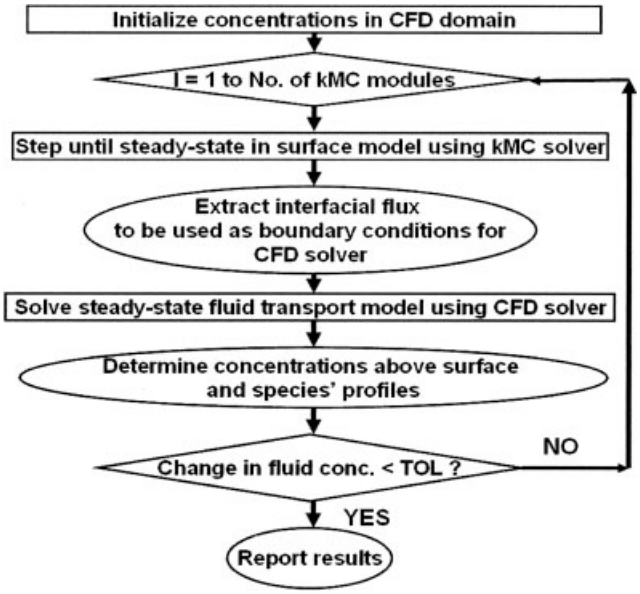

Figure 5. The iterative solution scheme used to obtain the steady-state solution using the multiscale scheme.

croscopic scale. A usual practice is to divide the lattice into smaller sublattices, and the occupancy in each of these sublattices is determined based on the gradient information.

Another important operator implemented in the gap-tooth scheme is "restriction", which is used to obtain the molar flux into the surface at the end of the kMC solution. During "restriction", the ensemble-based microscopic information is converted into dimensionless coverage. For species which exist in both free and adsorbed forms, this is straightforward, and Eq. 9 can be used directly to obtain the flux. For species which exist only in the fluid phase, for example, product C in the bimolecular mechanism, the expression $k_{Sf,kMC}\theta_{A-B}$ must be evaluated to obtain the interfacial flux (instead of $k_{Sf}\theta_A\theta_B$ as in the fully implicit model), where θ_{A-B} is the ratio of the number of AS-BS ensembles on the surface over the total number of lattice sites (which is 900 in the case of the 30×30 lattice used here), and $k_{Sf,kMC}$ is the forward rate constant for the surface reaction. Note that $k_{Sf,kMC} = k_{Sf}/8$ for the lattice configuration considered here,[72] and the interfacial flux for product C depends only on the rate of the forward surface reaction since k_{Sb} was set equal to zero. Once the interfacial molar fluxes for the different species were obtained at the positions of the different teeth, the overall coarse profile of the interfacial flux for the entire length of the reactor was obtained by interpolation. A single third-order polynomial was used for each species as the interpolating function for the entire length of the reactor, the coefficients of which were obtained by regression using the flux evaluated at the positions of the teeth through "restriction" as described earlier.

Coupling method

The three components discussed earlier are the essential components of the multiscale solution scheme. The strategy used to couple these components is discussed here.

Domain Decomposition Method. Recently, there has been considerable interest in the application of domain decomposition methods to the solution of partial differential equations.[73–75] In this approach, the domain of interest is partitioned into smaller subdomains to improve computational efficiency either by simplifying the generation of grids in an irregularly shaped domain, or by solving each of the domains separately in parallel. Another motivation for applying domain decomposition is if different subdomains are governed by different physics, and, thus, described by different equations.[67] Finally, it may be desirable to use different numerical schemes for solution of the different subdomains,[73] as is the case in the present work, which, thereby improves the overall efficiency of the solution.

In this problem, the reactor is broken down into two subdomains, the fluid domain and the surface domain. A finite-difference scheme is used to solve the fluid domain, while a kMC solver is used to solve the surface profile. The two domains are coupled together at the boundary by matching flux of the different species. Since the two solvers being implemented are suitable for different length- and time-scales, their solutions need to be interconverted efficiently and accurately. Interconversion is achieved using the lifting, restriction and interpolation operators as described earlier as parts of the gap-tooth scheme.

Iterative Solution Method. An iterative scheme is implemented to obtain the steady-state profiles using the domain decomposition method described earlier. The iterative method is shown in Figure 5. In this method, the concentration in the fluid phase throughout the entire length of the reactor is first initialized by solution of the model equations with surface coverages for all species at all values of z set equal to zero. Based on the fluid-phase concentrations at the interface, thus, obtained, all the surface modules are solved separately using kMC to obtain the steady-state configurations with identification of the steady state facilitated by the use of a second-order linear filter. Once the steady-state surface coverages are known, interfacial flux conditions are extracted to be used as boundary conditions for the fluid-phase solver. The fluid transport model is then solved subject to the new set of interfacial boundary conditions, and the new solution profile is compared with the previous solution. If the difference is less than a specified tolerance, convergence of the overall algorithm has been reached. The magnitude of the tolerance was fixed to 0.001 M for all the runs. If convergence has not been attained in this iteration, based on the new fluid-phase concentrations obtained at the interface, the surface modules are solved again to obtain the flux at the interface, and then the solution of the fluid phase is repeated.

Results and Discussion

The two different mechanisms described above were used to obtain the steady-state solutions using both the fully-implicit solution and the multiscale scheme. The results obtained using the two schemes are discussed here.

Unimolecular mechanism

Using both methods, solution was obtained for a reactor length of 1 μm. The inlet concentration of reactant A was

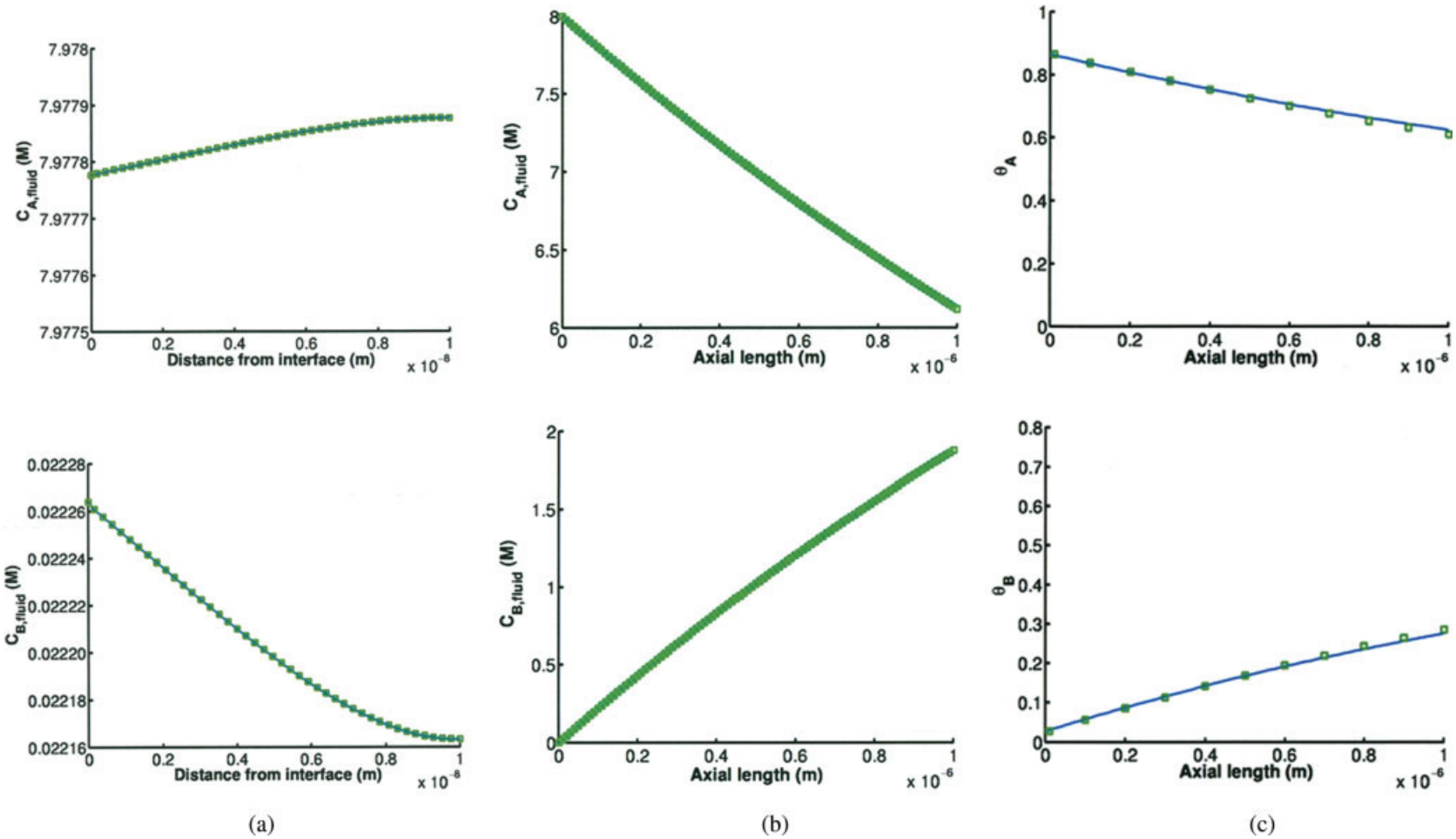

Figure 6. Comparison of solutions obtained using the fully implicit scheme, and the multiscale scheme for the unimolecular reaction mechanism.

The fully implicit solutions are shown as solid lines while the multiscale solution is shown as the symbols. The plots on the top show the concentration of reactant A in the radial direction along the second set of axial grid points (left), the concentration of A in the axial direction along the interface (middle), and the coverage of A in the axial direction (right). The figures on the bottom show the corresponding values for product B. It may be noted that the number of surface solutions obtained using the multiscale scheme is significantly lower than that using the fully implicit scheme. However, the use of interpolation enables the number of grid points solved in the fluid phase to be identical using both methods. The solutions obtained by the two methods are in excellent agreement. [Color figure can be viewed in the online issue, which is available at www.interscience.wiley.com.]

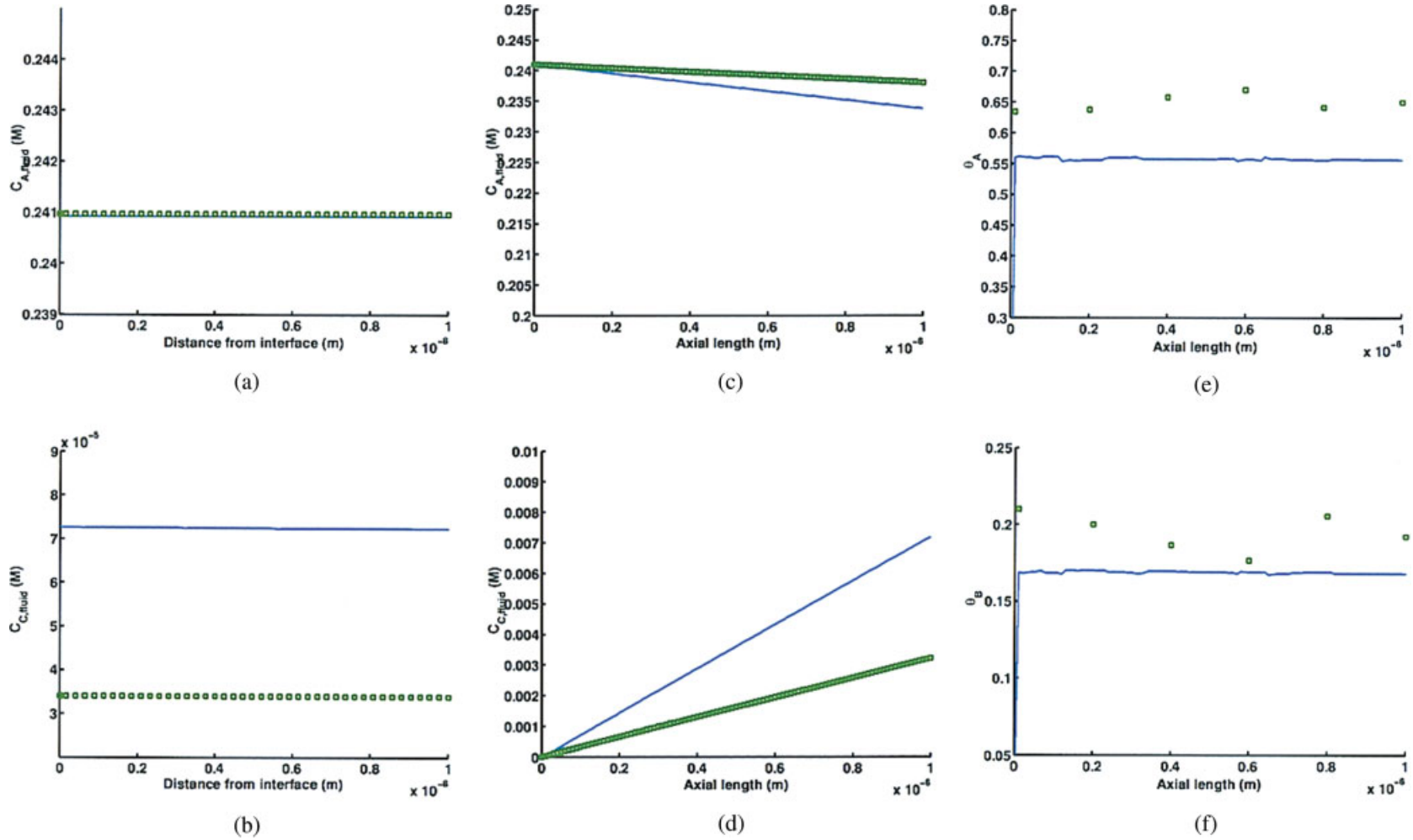

Figure 7. Comparison of solutions obtained using the fully implicit scheme and the multiscale scheme for the bimolecular reaction mechanism.

The fully implicit solutions are shown as solid lines, while the multiscale solution is shown as the symbols. (a) concentration of reactant A and (b) product C in the radial direction along the second set of axial grid points; (c) concentration of reactant A and (d) product C in the axial direction along the interface; coverage of (e) species A and (f) species B in the radial direction along the axial direction. Lack of agreement between the two solutions is the difference in the degree of surface diffusion in the two models. [Color figure can be viewed in the online issue, which is available at www.interscience.wiley.com.]

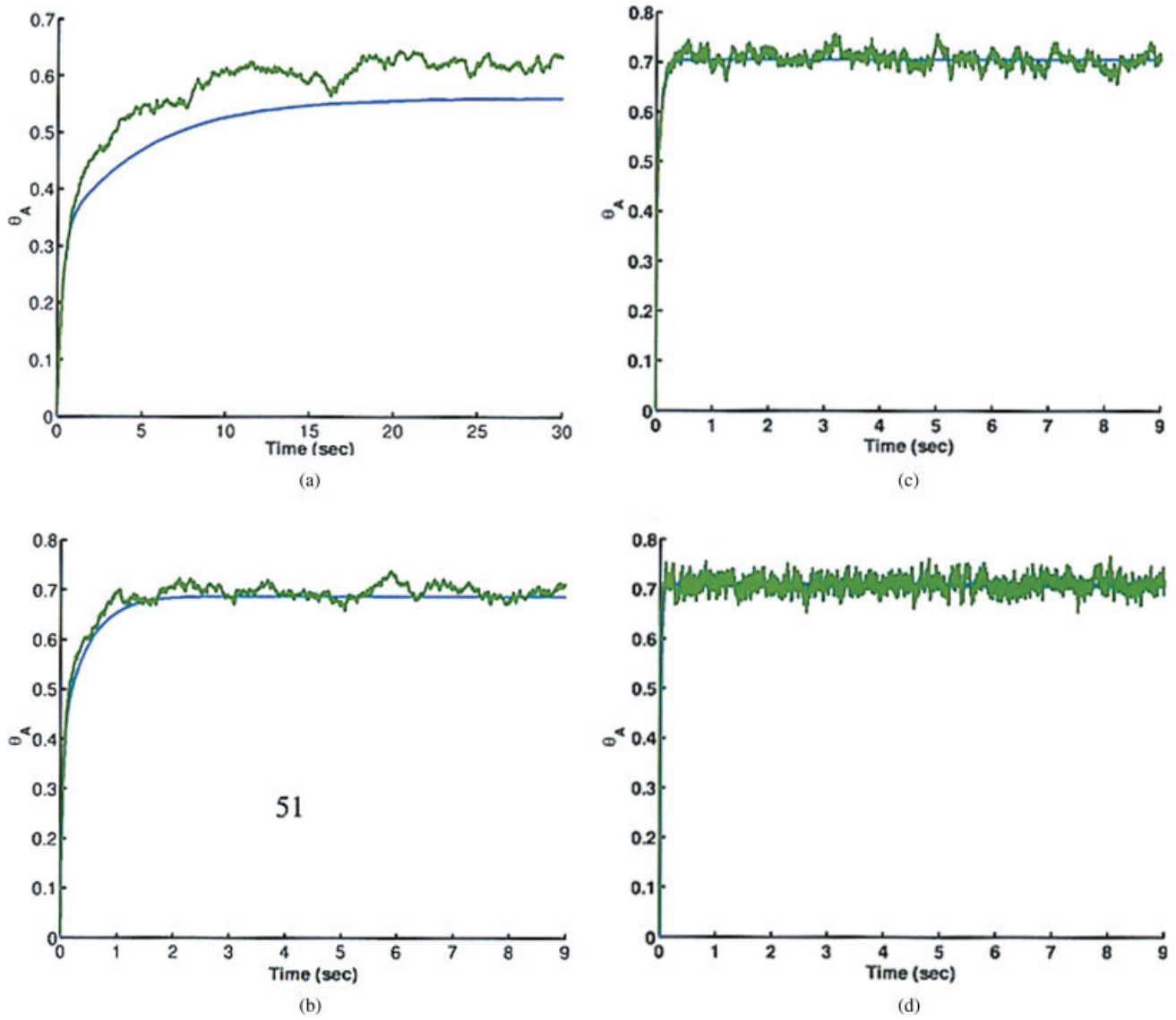

Figure 8. Comparison of transient profiles of the coverage of species A for the bimolecular reaction mechanism, obtained using the mean-field model and kinetic Monte Carlo for different magnitudes of surface diffusion (implemented by different rate constants of adsorption and desorption).

A 30 × 30 lattice (900 lattice sites) was used for each of the kMC runs. The mean-field solutions are shown as smooth solid lines, while the kMC solutions are characterized by fluctuations. All the profiles are obtained for fluid phase concentrations of 0.24 M for both A and B at the interface. (a) comparison at the original rate constants of adsorption and desorption; (b) comparison when the rate parameters for adsorption and desorption are 10 times the original; (c) comparison when the rate coefficients for adsorption and desorption are 50 times the original; (d) comparison when the rate coefficients for adsorption and desorption are 200 times the original rate constants. The two sets of solution are found to converge with increasing adsorption and desorption rate constants, which demonstrates the ability of kMC to capture heterogeneities due to low surface diffusion. This is manifested as deviations between the fully implicit and multiscale profiles for the bimolecular mechanism as shown in Figure 7. [Color figure can be viewed in the online issue, which is available at www.interscience.wiley.com.]

8 M and of product B was 0 M. In each case, concentrations were monitored at 101 sets of axial grids spaced 0.01 μm apart along the length of the reactor, with each axial set consisting of 86 nodal points for the two species present. Six different surface patches, spaced 0.2 μm apart, each of size 30 × 30, were simulated using the kMC solver in the multiscale scheme. For the given problem, the choice of six patches was based on a reasonable trade-off between computational speed and accuracy; the use of a smaller number of patches incorporates errors in the solution due to interpolation effects, and the use of a larger number of patches requires more computational time. While the computational time for each run varied due to the stochastic nature of the solution, an average run took about 20 iterations and 40 min to run on a workstation running a 2.2 GHz Xeon processor. About 1.0×10^6 events were simulated for each patch to attain steady state. Comparison of the results obtained for the multiscale scheme and the fully implicit solution is shown in Figure 6. Clearly, the two solutions are in very good agreement, thereby validating the implementation of the multiscale scheme.

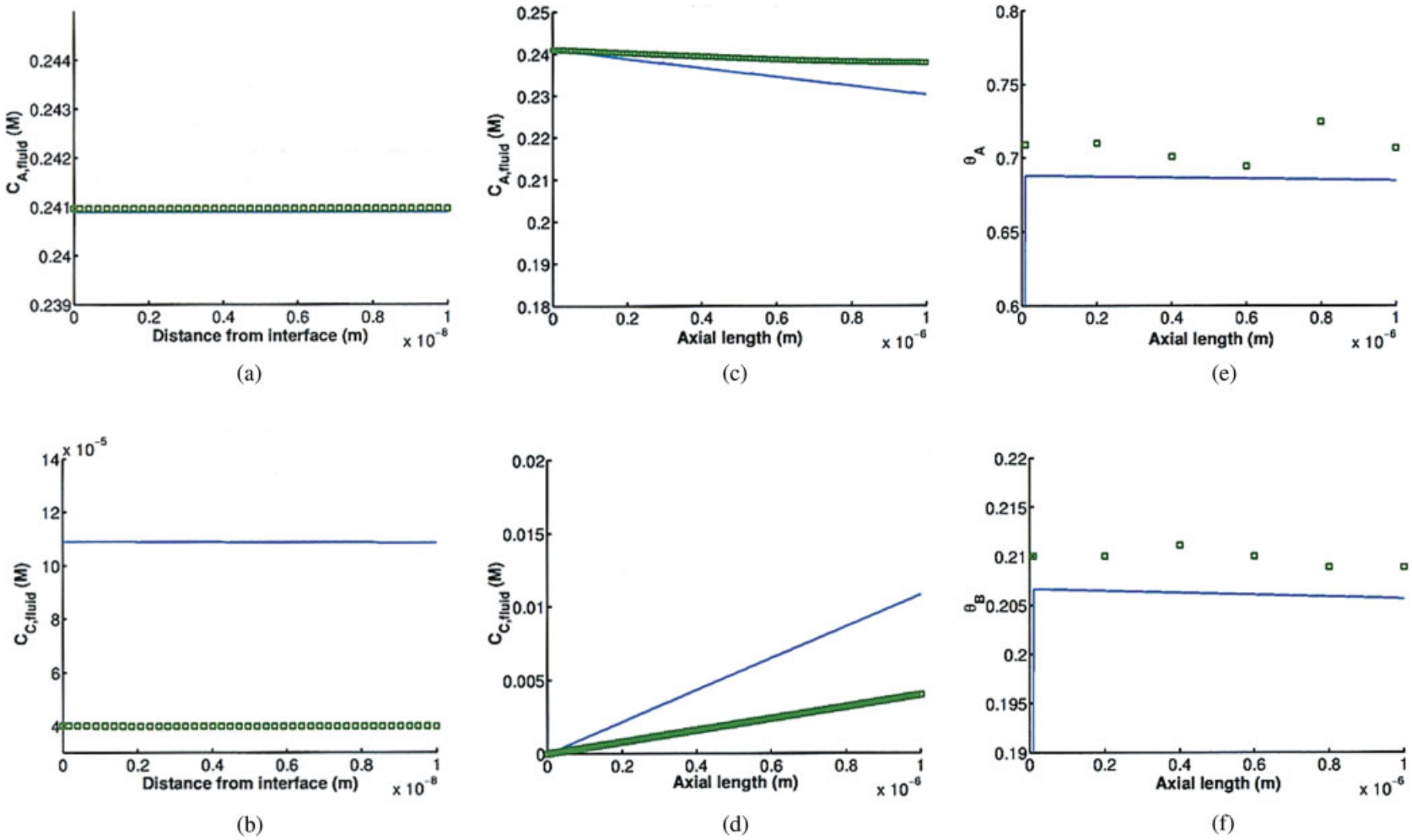

Figure 9. Comparison of solutions obtained using the fully implicit scheme and the multiscale scheme for the bimolecular reaction mechanism when the adsorption and desorption rate constants are 10 times the original (shown in Table 3).

The fully implicit solutions are shown as solid lines, while the multiscale solution is shown as the symbols. (a) concentration of reactant A and (b) product C in the radial direction along the second set of axial grid points; (c) concentration of reactant A and (d) product C in the axial direction along the interface; coverage of (e) species A and (f) species B in the radial direction along the axial direction. The two solutions are in better agreement than those shown in Figure 7 for lower values of the adsorption and desorption rate coefficients. [Color figure can be viewed in the online issue, which is available at www.interscience.wiley.com.]

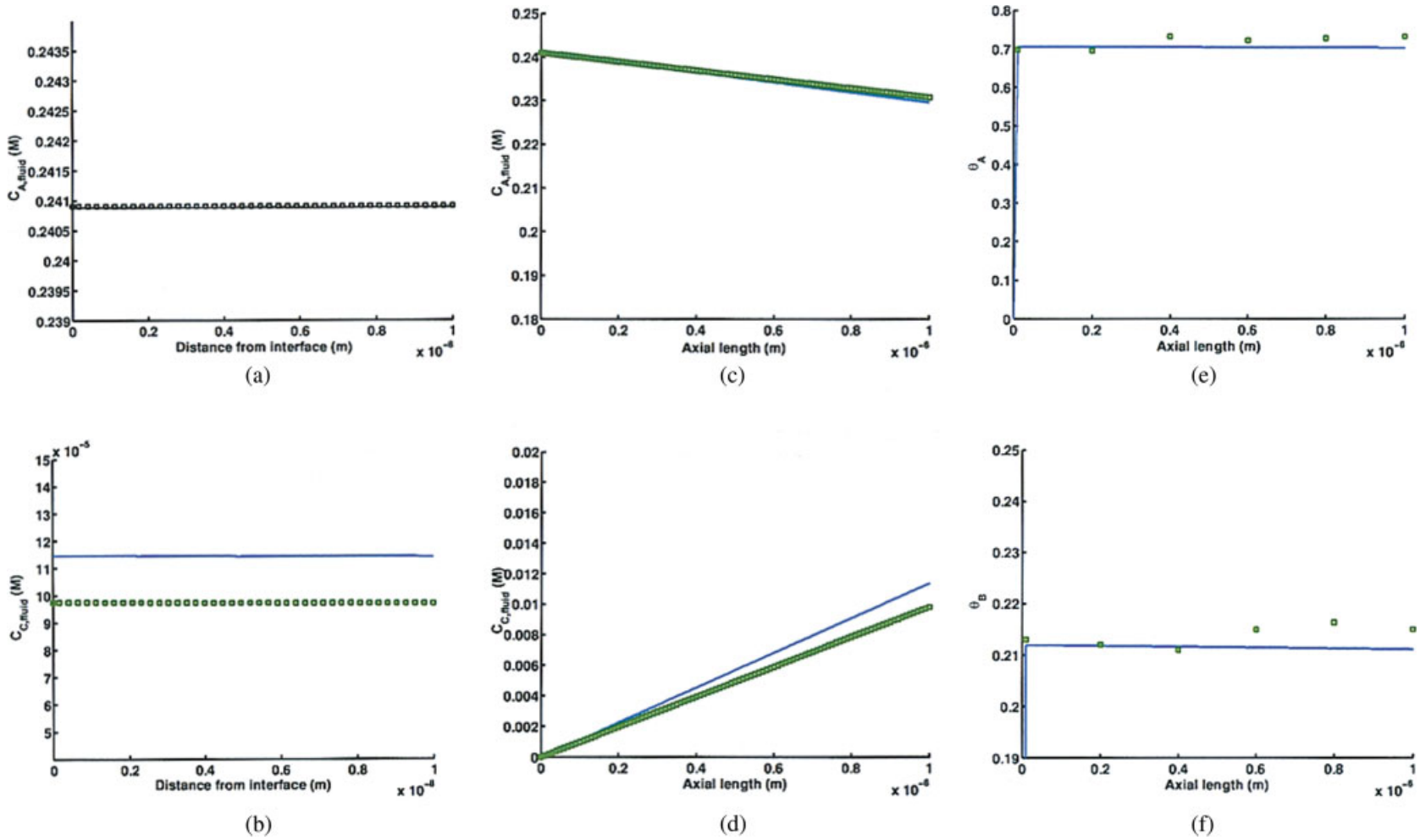

Figure 10. Comparison of solutions obtained using the fully implicit scheme and the multiscale scheme for the bimolecular reaction mechanism when the adsorption and desorption rate constants are 50 times the original (shown in Table 3).

The fully implicit solutions are shown as solid lines while the multiscale solution is shown as the symbols. (a) concentration of reactant A and (b) product C in the radial direction along the second set of axial grid points; (c) concentration of reactant A and (d) product C in the axial direction along the interface; coverage of (e) species A and (f) species B in the radial direction along the axial direction. The two solutions are in much better agreement than the solutions obtained using the original parameters (as shown in Figure 7). [Color figure can be viewed in the online issue, which is available at www.interscience.wiley.com.]

For the unimolecular reaction mechanism considered, the rate of surface diffusion does not play any role in determining the effective rates of adsorption, desorption and surface reaction. Therefore, although the mean-field model has an inherent assumption of infinite surface diffusion, and the kMC model does not account for any surface migration events, the rates predicted by both models are in complete agreement as expected.

Bimolecular mechanism

In the case of the bimolecular reaction mechanism, solutions were also obtained for a reactor of length 1 μm. The inlet concentrations of the reactants A and B were set at 0.24 M, while that of the product C was set to 0 M. For both solution schemes, concentrations were monitored at 101 sets of grid points placed 0.01 μm apart along the length of the reactor, with each axial set of grids consisting of 129 nodal points for the three species present. Six surface patches, each spaced 0.2 μm apart, were simulated using the kMC solver. As in the case of the unimolecular reaction mechanism, the choice of six patches placed 0.2 μm apart provided a reasonable trade-off between computational speed and accuracy. On average, a kMC run simulated about 2×10^6 events to reach steady state. A typical run took about 25 iterations and 2 h to converge. Comparison of the results obtained by the multiscale method and the fully implicit scheme is shown in Figure 7. The two solutions are found to disagree with each other. The fully-implicit model predicts a higher conversion than the multiscale scheme, while the coverage predicted by the multiscale model is higher than that predicted by the mean-field model. These results demonstrate how structural heterogeneities at the microscopic scale as implemented here via low surface diffusion can manifest themselves at the reactor scale. Although the conversion is low and the steady-state coverages do not vary appreciably along the length of the reactor, the surface heterogeneity manifests itself as significant and measurable differences in reactant conversion, product yields and surface coverages between the kMC and MF results.

For the bimolecular reaction mechanism considered, the net rate of the surface reaction is a strong function of the rate of surface diffusion. While the mean-field model considers infinite diffusion rates on the surface, the kMC model does not include any explicit surface diffusion events. Reaction is allowed only between first-nearest neighbors, thus, implying a low rate of surface diffusion. This leads to a lower effective rate of surface reaction than that predicted by the mean-field model. In order to explore this further, the temporal evolution of the adsorbate profiles at a single lattice position was studied using kMC and mean-field models for the same reaction mechanism and surface rate parameters, but with higher rate constants of adsorption and desorption. The profiles are shown in Figure 8. It was found that as the adsorption and desorption rate constants were increased, the agreement between the multiscale and the mean-field solutions improved, until finally when the rate parameters were over 200 times higher, the two solutions were in very good agreement. The fully-implicit solution and the multiscale solution for the entire reactor were also compared for the higher rate constants of adsorption and desorption. The results are shown in Figures 9 and 10 for factors of 10 and 50, respectively. A comparison of these figures with Figure 7 shows that the agreement between the fully-implicit solution and the multiscale solution at the reactor scale improves with increasing surface diffusion. These results further validate the implementation of the multiscale method. They also highlight the most attractive feature of the multiscale scheme, which is its ability to give a detailed description of the catalytic surface and its kinetics that allows surface nonuniformity to be taken into account. Furthermore, the multiscale method implemented here enables concentration variations in two spatial dimensions to be captured.

Conclusions

A multiscale algorithm was developed and implemented, which allows the solution of heterogeneous catalytic-flow reactors with resolution of concentration in the fluid phase in two dimensions. The scheme is implemented using a domain decomposition technique in which the fluid phase is solved using finite difference, while the catalyst phase is solved by a molecular-level solver implemented through a kinetic Monte Carlo scheme. Patches of kMC domains equally spaced in the axial direction were implemented along the surface of the reactor. A gap-tooth scheme was employed which performs lifting, restriction and interpolation operations to provide the complete set of boundary conditions along the physical interface, and is also responsible for initializing the lattice microstructures of the kMC domains, thereby ensuring efficient communication between the solvers at the different length- and time-scales.

Two sets of model kinetic mechanisms were solved using the multiscale scheme to obtain steady-state solutions. The first kinetic mechanism consisted of a single reactant and a product species participating in adsorption and desorption, along with a single unimolecular surface reaction step. The solution obtained using the multiscale scheme for this kinetic mechanism was found to be in very good agreement with a mean-field model solved using a fully implicit method. This agreement validates the implementation of the multiscale scheme. Furthermore, a second kinetic mechanism consisting of two reactants and one product species, which consists of a bimolecular surface reaction step, was also implemented. With the implementation of low surface diffusion by allowing only first nearest-neighbor interactions between adsorbates, the solution obtained by the multiscale scheme was found to differ significantly from the equivalent fully-implicit model, which demonstrates the capability of the multiscale model to track structural heterogeneities, such as low surface diffusion.

Acknowledgments

We gratefully acknowledge stimulating and helpful discussions with Prof. David Chopp. This work was supported by the National Science Foundation (CTS-0102612).

Literature Cited

1. Abraham FF. Portrait of a crack: Rapid fracture mechanism using parallel molecular dynamics. *IEEE Comp Sci and Eng*. 1997;4:66–77.

2. Abraham FF, Broughton JQ, Bernstein N, Kaxiras E. Spanning the length scales in dynamic simulation. *Comp in Phys*. 1998;12:538–546.
3. Armaou A, Kevrekidis IG, Theodoropoulos C. Equation-free gap-tooth-based controller design for distributed complex multiscale processes. *Comput Chem Eng*. 2005;29:731–740.
4. Bindal A, Ierapetritou MG, Balakrishnan S, Armaou A, Makeev AG, Kevrekidis IG. Equation-free, coarse-grained computational optimization using timesteppers. *Chem Eng Sci*. 2005;61:779–793.
5. Pablo JJ. Molecular and multiscale modeling in chemical engineering – current view and future perspectives. *AIChE J*. 2005;51:2372–2376.
6. Gang L, Kaxiras E. An overview of multiscale modeling of materials. *Condensed Matter*. 2004;preprint archive:1–28.
7. Gear CW, Kevrekidis IG. Boundary processing for Monte Carlo simulations in the gap-tooth scheme. physics/0211043 at arxiv.org. 2002.
8. Gear CW, Li J, Kevrekidis IG. The gap-tooth method in particle simulations. *Phys Lett A*. 2003;316:190–195.
9. Gungor MR, Gray LJ, Zhou SJ, Maroudas D. Modeling of failure in metallic thin films induced by stress and electromigration: a multiscale computational analysis. *Mat Res Soc Symp Proc*. 1999;538: 263–268.
10. Jensen KF, Rodgers ST, Venkataramani R. Multiscale modeling of thin film growth. *Curr Opinion in Solid State Mat Sci*. 1998;3:562–569.
11. Kevrekidis IG, Gear CW, Hummer G. Equation free: The computer-aided analysis of complex multiscale systems. *AIChE J*. 2004;50: 1346–1353.
12. Kevrekidis IG, Gear CW, Hyman JM, Kevrekidis PG, Runborg O, Theodoropoulos C. Equation-free multiscale computation: Enabling microscopic simulators to perform system-level tasks submitted to *Comm Math Sci*. physics/0209043 at arxiv.org.2002.
13. Maroudas D. Multiscale modeling of hard materials: challenges and opportunities for chemical engineering. *AIChE J*. 2000;46: 878–882.
14. Rudd RE, Broughton JQ. Concurrent coupling of length scales in solid state systems. *Physica Status Solidi B Basic Res*. 2000;217: 251–291.
15. Shenoy V, Miller R, Tadmor EB, Rodney D, Phillips R, Ortiz M. An adaptive methodology for atomic scale mechanics – the quasi-continuum method. *J Mech Phys Sol*. 1999;47:611–642.
16. Shilkrot LE, Curtin WA, Miller RE. A coupled atomistic/continuum model of defects in solids. *J Mechanics and Phys of Solid*. 2002;50: 2085–2106.
17. Yip S. Synergistic science. *Nature Materials*. 2003;2:3–5.
18. Zepeda-Ruiz LA, Maroudas D, Weinberg WH. Theoretical study of the energetics, strain fields, and semicoherent interface structures in layer-by-layer semiconductor heteroepitaxy. *J App Phys*. 1999;85: 3677–3695.
19. Baldini L, Hunter CA. Self-assembly of porphyrin arrays. *Adv Inorg Chem*. 2002;53:213–259.
20. Barth JV, Constantini G, Kern K. Engineering atomic and molecular nanostructures at surfaces. *Nature*. 2005;437:671–679.
21. Eigler DM, Schweizer EK. Positioning single atoms with a scanning tunnelling microscope. *Nature*. 1990;344:524–526.
22. Gates BD, Xu Q, Stewart M, Ryan D, Wilson CG, Whitesides GM. New approaches to nanofabrication: molding, printing and other techniques. *Chem Rev*. 2005;105:1171–1196.
23. Huie JC. Guided molecular self-assembly: A review of recent efforts. *Smart Mat Struct*. 2003;12:264–271.
24. Junno T, Deppert K, Montelius L, Samuelson L. Controlled manipulation of nanoparticles with an atomic force microscope. *Appl Phys Lett*. 1995;66:3627–3629.
25. Kim P, Lieber CM. Nanotube nanotweezers. *Science*. 1999;286: 2148–2150.
26. Lazzari M, Lopez-Quintela MA. Block copolymers as a tool for nanomaterial fabrication. *Adv Mater*. 2003;15:1583–1594.
27. Lehn JM. Toward self-organization and complex matter. *Science*. 2002;295:2400–2403.
28. Li M, Schnablegger H, Mann S. Coupled synthesis and self-assembly of nanoparticles to give structures with controlled organization. *Nature*. 1999;402:393–395.
29. Messmore BW, Sukerkar PA, Stupp SI. Mirror image nanostructures. *J Amer Chem Soc*. 2005;127:7992–7993.
30. Niemeyer CM. Tools for the biomolecular engineer. *Science*. 2002; 297:62–63.
31. Shedd GM, Russell PE. The scanning tunneling microscope as a tool for nanofabrication. *Nanotechnology*. 1990;1:67–80.
32. Whitesides GM, Mathias JP, Seto CT. Molecular self-assembly and nanochemistry: a chemical strategy for the synthesis of nanostructures. *Science*. 1991;254:1312–1319.
33. Wiesendanger R. *Scanning Probe Microscopy and Spectroscopy*. Cambridge, UK: Cambridge University Press; 1994.
34. Zeppenfeld P, Lutz CP, Eigler DM. Manipulating atoms and molecules with a scanning tunneling microscope. *Ultramicroscopy*. 1992;42: 128–133.
35. Belanger S, Hupp JT. Porphyrin-based thin-film molecular materials with highly adjustable nanoscale porosity and permeability characteristics. *Angew Chem Int Ed Eng*. 1999;38:2222–2224.
36. Yaghi OM, O'Keeffe M, Ockwig N, Chae HK, Eddaoudi M, Kim J. Reticular synthesis and the design of new materials. *Nature*. 2003;423:705–714.
37. Cho S, Walther ND, Nguyen ST, Hupp JT. Anodic aluminium oxide catalytic membranes for asymmetric epoxidation. *Chem Commun*. 2005;42:5331–5333.
38. Ciardelli C, Nova I, Tronconi E, Konrad B, Chatterjee D, Ecke K, Weibel M. SCR-DeNO_x for diesel engine exhaust aftertreatment: Unsteady-state kinetic study and monolith reactor modeling *Chem Eng Sci*. 2004;59:5301–5309.
39. Desai FN, Greene HL, Subbanna P. Catalytic oxidation of decomposition products from spent ion-exchange resins. *Ind Eng Chem Res*. 1987;26:1965–1969.
40. Machado RM, Booekhuis RR, Nordquist AF, Roy BP, Carney SR. Applying monolith reactors for hydrogenations in the production of speciality chemicals – process and economic considerations. *Catalysis Today*. 2005;105:305–317.
41. Schildhauer TJ, Tromp S, Mueller I, Schilkin A, Kenig EY. Modeling of reactive stripping in monolith reactors. *Catalysis Today*. 2005;105:414–420.
42. Trevino C, Sen M. Catalytic combustion in monolith reactors. *Chem Eng Sci*. 1986;41:2253–2260.
43. Bhattacharya M, Harold MP, Balakotaiah V. Mass-transfer coefficients in washcoated monoliths. *AIChE J*. 2004;50:2939–2955.
44. Jirat J, Kubicek M, Marek M. Mathematical modelling of catalytic monolithic reactors with storage of reaction components on the catalytic surface. *Catalysis Today*. 1999;53:583–596.
45. Jirat J, Stepanek F, Kubicek M, Marek M. Nonstationary operation of a system of catalytic monolith reactors for selective NO_x reduction. *Chem Eng Sci*. 1999;54:2609–2618.
46. Koci P, Kubicek M, Marek M. Modeling of three-way-catalyst monolith converters with microkinetics and diffusion in the washcoat. *Ind Eng Chem Res*. 2004;43:4503–4510.
47. Koci P, Kubicek M, Marek M. Periodic forcing of three-way catalyst with diffusion in the washcoat. *Catalysis Today*. 2004;98:345–355.
48. Koci P, Marek M, Kubicek M, Maunula T, Harkonen M. Modelling of catalytic monolith convertors with low- and high-temperature NO_x storage compounds and differential washcoat. *Chem Eng J*. 2004;97:131–139.
49. Ramanathan K, Balakotaiah V, West DH. Light-off criterion and transient analysis of catalytic monoliths. *Chem Eng Sci*. 2003;58: 1381–1405.
50. Wanker R, Raupenstrauch H, Staudinger G. A fully distributed model for the simulation of a catalytic combustor. *Chem Eng Sci*. 2000;55:4709–4718.
51. Bauer M, Schreier M, Nowak U, Adler R. A two-phase model for the mathematical modeling of heterogeneous gaseous catalytic fixed-bed reactor. *Chemische Technik (Leipzig)*. 1998;50:169–176.
52. Champagnie AM, Tsotsis TT, Minet RG, Wagner E. The study of ethane dehydrogenation in a catalytic membrane reactor. *J Catal*. 1992;134:713–730.
53. Neomagus HW, Saracco G, Wessel HF, Versteeg GF. The catalytic combustion of natural gas in a membrane reactor with separate feed of reactants. *Chem Eng J*. 2000;77:165–177.
54. Nir A, Pismen LM. Simultaneous intraparticle forced convection, diffusion and reaction in a porous catalyst. *Chem Eng Sci*. 1977; 32:35–41.
55. Ramachandran PA. Application of the boundary element method to nonlinear diffusion with reaction problems. *Int J Num Methods Eng*. 1990;29:1021–1031.

56. Salmi T, Warna J. Modeling of catalytic packed-bed reactors – comparison of different diffusion models. *Comput Chem Eng*. 1991;15:715–727.
57. Sanchez J, Tsotsis TT. Current developments and future research in catalytic membrane reactors. *Mem Sci Tech*. 1996;4:529–568.
58. Sousa JM, Cruz P, Mendes A. Modeling a catalytic polymeric nonporous membrane reactor. *J Mem Sci*. 2001;181:241–252.
59. Sousa JM, Cruz P, Mendes A. A study on the performance of a dense polymeric catalytic membrane reactor. *Catalysis Today*. 2001; 67:281–291.
60. Sousa JM, Mendes A. Simulating catalytic membrane reactors using orthogonal collocation with spatial coordinates transformation. *J Mem Sci*. 2004;243:283–292.
61. Wu S, Gallot JE, Bousmina M, Bouchard M, Kaliaguine S. Zeolite containing catalytic membranes as interphase contactors. *Catalysis Today*. 2000;56:113–129.
62. Yawalkar AA, Pangarkar VG, Baron GV. Alkane epoxidation with peroxide in a catalytic membrane reactor: A theoretical study. *J Mem Sci*. 2001;182:129–137.
63. Majumder D, Broadbelt LJ. Development and comparison of solution methods for modeling reaction and diffusion in molecular square membrane. *Ind Eng Chem Res*. 2005;44:5977–5986.
64. Lam R, Vlachos DG. Multiscale model for epitaxial growth of films: Growth mode transition. *Phys Rev B*. 2001;6403:396–404.
65. Lou Y, Christofides PD. Estimation and control of surface roughness in thin film growth using kinetic Monte-Carlo models. *Chem Eng Sci*. 2003;58:3115–3129.
66. Rusli E, Drews TO, Braatz RD. Systems analysis and design of dynamically coupled multiscale reactor. *Chem Eng Sci*. 2004;59:5607–5613.
67. Vlachos DG. Multiscale integration algorithms for homogeneous-heterogeneous reactors *AIChE J*. 1997;43:3031–3041.
68. Karger J, Ruthven DM. *Diffusion in zeolites and other microporous solids*. New York: John Wiley and Sons; 1992.
69. Geankoplis CJ. *Transport processes and unit operations*. Boston: Allyn and Bacon; 1983.
70. Cussler EL. *Diffusion: Mass transfer in fluid systems*. Cambridge, UK: Cambridge University Press; 1997.
71. Pollard WG, Present RD. On gaseous self-diffusion in long capillary tubes. *Phys Rev*. 1948;73:762–774.
72. Dooling DJ, Broadbelt LJ. Generic Monte Carlo tool for kinetic modeling. *Ind Eng Chem Res*. 2001;40:522–529.
73. Kurz S, Becker U, Maisch H. Dynamic simulation of electromechanical systems: From Maxwell's theory to common-rail diesel injection. *Naturwissenschaften*. 2001;88:183–192.
74. Pfeiffer HP, Kidder LE, Scheel MA, Teukolsky SA. A multidomain spectral method for solving elliptic equations. *Comput Phys Commun*. 2003;152:253–273.
75. Smith B, Bjorstad P, Gropp W. *Domain decomposition*. Cambridge University Press; 1996.

Manuscript received Mar. 24, 2006, and revision received Aug. 31, 2006.